Materials & Design 250 (2025) 113585

Contents lists available at ScienceDirect

Materials & Design

journal homepage: www.elsevier.com/locate/matdes

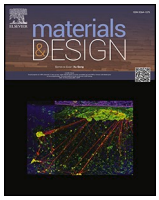

Deformation induced microstructure of stress relieved Zircaloy-4 cladding

Malachi Nelson [a,b,*], Shmuel Samuha [a,c], Dina Sheyfer [d], David Kamerman [b], David Yang [e,f], Kay Song [e], Felix Hofmann [e], Jon Tischler [d], Peter Hosemann [a]

[a] University of California Berkeley – Department of Nuclear Engineering Berkeley CA USA
[b] Idaho National Laboratory – Fuel Development, Performance, and Qualification Idaho Falls ID USA
[c] NRCN – Department of Materials Engineering Beer-Sheva Israel
[d] Argonne National Laboratory – X-ray Science Division Lemont IL USA
[e] University of Oxford – Department of Engineering Science Oxford United Kingdom
[f] Brookhaven National Laboratory – Condensed Matter Physics and Materials Science Department, Upton NY USA

ARTICLE INFO

Keywords:
Fuel Cladding
Zircaloy
Microstructure
Mechanical Anisotropy

ABSTRACT

This work evaluates the microstructural evolution of cold-worked, stress-relieved Zircaloy-4 cladding from pristine to uniaxial and biaxial deformed states. Differential aperture Laue diffraction and electron backscatter diffraction techniques are used to characterize intragranular strains, strain gradients, and grain fragmentation as metrics of deformation microstructure. The effects of mechanical anisotropy on deformation microstructure are investigated by comparing characterization results of samples subjected to different applied loads, including biaxial internal pressure and uniaxial tension along the rolled direction at 400 °C. Quantitative comparisons are made between the pristine microstructure and deformation-induced microstructure under both loading modes. Viscoplastic self-consistent simulations are performed to further investigate the microstructural evolution. Results indicate that biaxial loading from internal pressurization increases the deformation microstructure more than uniaxial loading along the rolled direction due to the relationship between loading and texture symmetry. Additionally, characterization results and simulations show distinct deformation-induced micro-textures: axial loading promotes a prismatic $\{10.0\}$ fiber texture in the rolled direction, which strengthens the micro-texture inherited from pilgering, whereas pressure loading results in a $\{2\bar{1}.0\}$ texture fiber, weakening the original micro-texture inherited from pilgering.

1. Introduction

Nuclear fuel cladding in light water reactor conditions can be exposed to inelastic deformation during anticipated operational occurrences such as pellet-cladding interaction (PCI) or fission gas release scenarios. Inelastic deformation changes material microstructure, usually by generating dislocations that propagate slip, forming microscopic strain and rotation gradients compatible with the macroscopic strain. Defects such as vacancies, interstitials, grain boundaries, and other dislocations can obstruct dislocation glide which increases the material strength but reduces ductility. These microstructural changes are crucial to the performance and failure limits of nuclear fuel cladding [1] and can improve fuel performance simulations through material models that account for cold-work factors and cumulative damage fractions [2].

Light water reactor cladding applications widely use zirconium alloys, which have a hexagonal close packed (HCP) crystal structure and slip systems with differing properties [3]. This results in a preferential crystallographic texture forming during manufacturing, commonly retained to improve the cladding strength and resistance to thinning [3]. Pilgering seamless cladding tubes and rolling flat plates produces similar textures with characteristic properties in the rolling direction (RD), transverse direction (TD), and normal direction (ND) which correspond to the axial, hoop, and radial directions in cladding tubes, respectively. HCP microstructure plasticly deformed using these forming techniques results in a strong basal (00.2) texture fiber in the ND and prismatic $\{10.0\}$ fiber in the RD, but recrystallization causes the basal planes to rotate by $\pm 30^{\circ}$ about the *c*-axis changing the RD fiber to $\{2\bar{1}.0\}$ [3,4]. Cold-worked, stress-relieved (CWSR) annealing partially recrystallizes the cladding after pilgering but retains some cold-worked microstructure to achieve higher strength and is often used for pressurized water reactor cladding [5,6]. This produces a bimodal microstructure: the recrystallized (RX) fraction displays $\{2\bar{1}.0\}$ texture in the RD with low

* Corresponding author at: Mail Stop 3805, 2525 Fremont Ave, Idaho Falls, ID 83401, USA.
E-mail address: malachi.nelson@inl.gov (M. Nelson).

https://doi.org/10.1016/j.matdes.2025.113585
Received 19 July 2024; Received in revised form 21 November 2024; Accepted 2 January 2025
Available online 6 January 2025

intragranular misorientation, and the residual cold-worked fraction displays {10.0} texture in the RD with high intragranular misorientation [4].

Uniaxial mechanical testing is commonly used to measure mechanical behavior of materials, including research on anisotropic textured Zircaloys [7–12]. However, PCI conditions produce biaxial loading with an axial/hoop stress ratio of approximately 0.75 [13,14]. Previous research has demonstrated that internal pressure loading better emulates the resolved shear stress distribution of PCI conditions compared to uniaxial loading in the RD, which affects the mechanical behavior of the cladding [15]. Prior microstructure characterization suggested that the deformation microstructure, such as residual strain and intragranular misorientation, is also sensitive to the applied loading mode: for the same equivalent strain, the sample deformed *via* internal pressure displayed signs of increased deformation microstructure compared to the sample deformed *via* uniaxial tension in the RD [16].

Viscoplastic self-consistent (VPSC) simulations can aid in relating mechanical and microstructural results by modeling the deformation activity of a material responding to an applied load and predicting useful data such as texture evolution and plastic spin. Plastic spin is an effect of continuum plasticity in polycrystalline materials where volumes of microstructure are required to rotate in different directions *via* dislocation slip to maintain continuity across grain boundaries during plastic deformation [17,18]. Rotation can occur at various length-scales, encompassing multiple grains, a single grain, or even small crystallites within a grain, but plastic spin specifically refers to non-coaxial rotation from the macroscopic rotation due to plastic slip alone [17,19,20]. Plastic spin is an important consideration for anisotropic materials at high strains, particularly those with HCP structures [18–21].

Zircaloys are challenging to characterize because the soft metal galls easily during metallographic preparation and an oxide layer can quickly form in air between polishing and characterization. CWSR Zircaloy-4 (Zry-4) presents an even greater challenge due to small grains, high residual strains, and high intragranular misorientation [22]. The existing cold-worked microstructure from manufacturing can obscure the microstructural evolution resulting from plastic deformation. This study investigates the deformation microstructure of CWSR Zry-4 cladding in the pristine and deformed states using differential aperture Laue diffraction and electron backscatter diffraction (EBSD) techniques. A sample deformed using biaxial internal pressure loading is characterized in detail alongside a pristine sample to reveal how inelastic deformation modifies CWSR microstructure under PCI conditions. These results are compared to a sample deformed by uniaxial tension in the RD to evaluate the effects of mechanical anisotropy on microstructure evolution. The effect of differing RD, TD, and ND strain ratios from the applied loading modes are studied using VPSC modeling. This comparison aims to clarify if and under what conditions uniaxial microstructure is representative of biaxial deformation induced microstructure.

2. Materials and methods

Samples characterized in this study are selected from CWSR Zry-4 cladding tested in [23]. In this study, Zry-4 cladding was cut into 15 cm segments and loaded using axial tension and internal pressure to high strains with axial and transverse extensometers to provide known strains for the gauge section. Samples were heated in a furnace in an argon atmosphere for one hour at temperature before applying 0.1 % per minute (1.67×10^{-5}/s) monotonic axial and hoop strain rates for axial tension and internal pressure loading, respectively. A more detailed description of the mechanical testing system and methods is provided in [23]. These mechanical testing sample provide prototypic cladding deformed with different applied stresses used for this analysis of microstructure anisotropy.

Samples are selected from [23] aiming to procure a sample deformed at elevated temperature using full-tube axial tension, with increased work hardening effects compared to a similar sample deformed using internal pressure. An undeformed sample is also characterized to compare the pristine microstructure with the deformation-induced microstructures of samples subjected to the biaxial and uniaxial loading modes. These samples are described using their biaxial-deformed, uniaxial-deformed, and pristine states hereon. The cladding material is from the same batch of cladding as [15,16,23] and is described further therein. The von Mises effective stress (σ_{eff}) and equivalent strain (ϵ_{eq}) are used to compare stress and strain from different loading modes assuming no shear components as shown in Equation (1) and Equation (2) [24]. Table 1 provides a summary of relevant sample properties.

$$\sigma_{\text{eff}} = \sqrt{\frac{(\sigma_z - \sigma_\theta)^2 + (\sigma_\theta - \sigma_r)^2 + (\sigma_r - \sigma_z)^2}{2}} \tag{1}$$

$$\epsilon_{\text{eq}} = \sqrt{\frac{2}{9}\left((\epsilon_z - \epsilon_\theta)^2 + (\epsilon_\theta - \epsilon_r)^2 + (\epsilon_r - \epsilon_z)^2\right)} \tag{2}$$

Samples are prepared for characterization by cutting the gauge sections of the cladding tubes into smaller pieces using a SiC cutoff saw blade cooled with water. These pieces are then subjected to a mechanical grinding process with SiC papers of varying coarseness (400, 600, 800 grit) to reveal the RD-TD plane. This plane forms the sample surface as shown in Fig. 1 (a) and is oriented such that its normal vector is aligned with the ND axis of the cladding. Following the grinding process, the samples are polished using diamond lapping films with particle sizes of 3 μm and 1 μm, respectively. The final polishing step involves a chemical–mechanical process using a 20 nm colloidal silica solution for 30 min. Residual strains from polishing are removed using cryo-electropolishing conducted for 1 min using the following conditions: solution (93 vol% ethanol, 7 vol% perchloric acid), and electropolishing parameters (0 °C, 95 mA, 25 V).

The 3D X-ray Microscope (3DXM) used for the Laue diffraction in this work is located at Argonne National Laboratory (ANL) in the Advanced Photon Source (APS) synchrotron, beamline 34-ID-E. The 3DXM performs Laue micro-diffraction using a focused beam with a differential aperture and area detectors to illuminate and reconstruct sub-micron voxels in three dimensions. The Laue diffraction patterns corresponding to each voxel in the sample are used to determine the localized orientation and deviatoric lattice strain tensor. A photograph of the beamline is included in Fig. 1 (b) and further discussion of this technique is available in [25,26].

This study primarily employs the polychromatic x-ray beam with an energy range of 7–30 keV, focused using a pair of Kirkpatrick-Baez (KB) mirrors to approximately 300 × 300 nm^2 with a flux of about 10^{11} photons/s. Laue diffraction patterns are collected by the pixel-array Perkin-Elmer detector (2048 × 2048 pixel grid, 200 × 200 μm^2 pixel size) positioned about 500 mm above the sample centered at a scattering angle of 90°. The geometry of the detector and wire are calibrated using a strain-free 5 μm thick silicon wafer [27]. The Zry-4 sample is mounted in a 45° reflection geometry as shown in Fig. 1 (a), so the cladding RD, TD, and ND correspond with the H, X, and F axes, respectively. Sample structure is imaged in the X-Z plane with 0.5 μm resolution by analyzing Laue diffraction patterns collected with an exposure time of one and two seconds for pristine and deformed Zry-4 samples, respectively, in a 2D scan. At each sample X position, a differential aperture scan is performed by moving wire along the H direction across the diffracted X-rays to

Table 1
Mechanical testing parameters of characterized samples.

Samples	Temperature	Loading Mode	$\frac{\sigma_{RD}}{\sigma_{TD}}$	$\epsilon^p_{RD} : \epsilon^p_{TD} : \epsilon^p_{ND}$	ϵ^{tot}_{eq} max.
Pristine	–	–	–	–	0 %
Biaxial-Deformed	400 °C	Internal Pressure	0.5	−2.43: 16.1: −15.7 ($\times 10^{-6}$/s)	4.2 %
Uniaxial-Deformed	400 °C	Axial Tension	∞	16.0: −11.8: −3.75 ($\times 10^{-6}$/s)	5.1 %

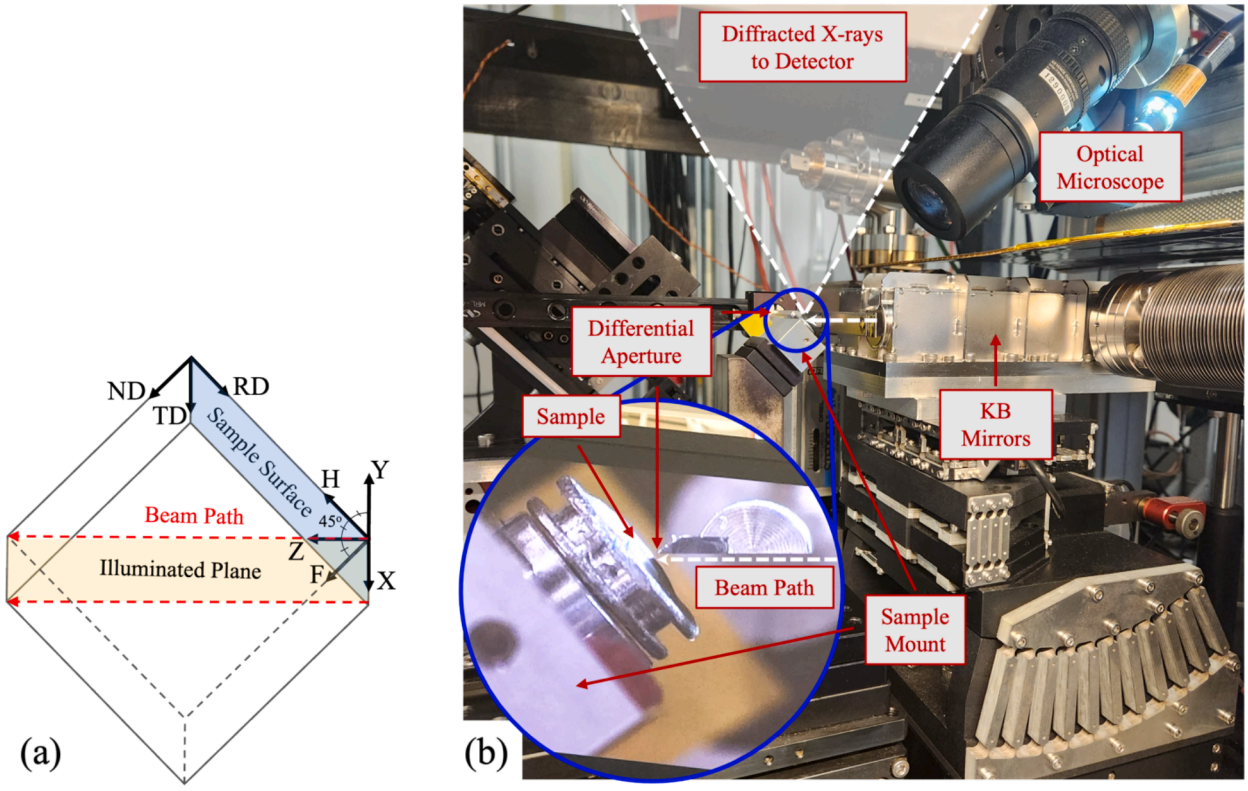

Fig. 1. (a) Schematic of the sample coordinate system (X, H, F) and the beamline coordinate system (X, Y, Z). (b) Photograph of the APS beamline 34-ID-E with an inlay showing the sample target and differential aperture.

resolve diffracted signals from sample along Z. Depth-resolved Laue pattern reconstructions and Laue diffraction peak indexing are performed using the high-performance computing cluster at ANL. An example of a depth resolved Laue pattern is included in the Supplemental materials (Fig. S1). Lattice parameters, *a* and *c*, are measured in the pristine sample using monochromatic energy scans across relevant spectra to determine the photon energy with the strongest diffraction conditions. Three independent diffraction peaks, $(\bar{1}2.4)$, $(\bar{2}3.5)$, and $(\bar{3}3.8)$, are scanned in this manner to measure the lattice parameters and an example is included in the Supplementary materials (Fig. S2). Local deviatoric lattice strain is calculated and visualized using Igor Pro 9 and MATLAB R2020b. Due to beamline availability, only the pristine and biaxial-deformed samples are characterized using 3DXM.

EBSD characterization is performed using a ThermoFisher Scientific Scios 2 DualBeam scanning electron microscope coupled with a Symmetry S3 EBSD detector (Oxford Inc.). The EBSD acquisitions are performed with the sample surface highlighted in Fig. 1 (a) at 70° tilt to the beam axis, using a 6.4nA current at an accelerating voltage of 20 kV and a working distance of 15 mm. Scans parameters are included in the Supplementary materials (Table S1). EBSD data are processed using the software ATEX by [28], v. 14. Grain boundaries are defined where misorientation from the nearest neighbors is greater than 10° and Grain sizes (*d*) for EBSD and 3DXM methods are calculated using the surface area (*S*) of the grain according to Equation (3). Kernel average misorientation (KAM) measures orientation gradients indicative of strain and is used as a short-range metric of deformation, while the disorientation from average orientation (DAO) measures compounded misorientation and is used as a long-range metric of deformation. KAM is used to determine the RX fractions where the average and maximum KAM within a grain must be less than 2° and 5°, respectively.

$$d = 2 \bullet \sqrt{\frac{S}{\pi}} \tag{3}$$

The texture and grain morphology of the pristine cladding from EBSD datasets at all magnifications are used to perform VPSC simulations using the software ATEX by [28], v. 14. The pristine microstructure is used to provide identical initial conditions and the strain rates provided in Table 1 are used to define the macroscopic velocity gradient tensor for 5 % strain. In addition to modeling the internal pressure and RD tension velocity tensors, a TD tension velocity tensor is simulated using the RD tension velocity tensor with the RD and TD rates switched. These strain rates may not perfectly represent experimental strain rates of uniaxial tension in the TD, but Wang & Murty [29] show that Zry-4 anisotropy constants are similar at 400 °C indicating that this assumption is applicable. The uniaxial-TD simulation is performed to investigate differences between uniaxial and multiaxial loading versus uniaxial loading-texture orientation.

Prismatic type I $\{10.0\}\langle 1\bar{2}.0\rangle$, basal $\langle 00.2\rangle\langle 1\bar{2}.0\rangle$, and pyramidal type I $\{10.1\}\langle 2\bar{1}.\bar{3}\rangle$ slip system families are simulated to include the primary slip systems active in Zr and Zircaloys [3,30,31]. The relative strength of each slip system is calculated at 400 °C using equations for critical resolved shear stresses provided in [7,30], with the prismatic, basal, and pyramidal systems achieving relative strengths of 1, 3.2, and 7.7, respectively. Further discussion of the relevance of these slip systems and the temperature-dependent equations for the critical resolved shear stresses is included in [15]. The self-consistent model is chosen with dislocation cell hardening while all other values are left default. All simulation variables other than the macroscopic velocity gradient tensor are identical for each simulation and are available in the Supplementary materials (Fig. S3).

3. Results

3.1. 3DXM

The basal (00.2) orientation characteristics of the pristine and

biaxial-deformed samples are shown in Fig. 2. The orientation data are presented in the sample coordinate system using ND projection pole figures with each voxel directly projected on the pole figure. The inverse pole figure (IPF) micrographs show the indexed voxels of the illuminated plane displaying the orientation data using the ND pole figure coloring. Fig. 1 (a) helps relate the RD-TD axes used to display the ND projection of the sample surface and the X-Z axes of the illuminated plane. The 3DXM acquires a relatively high index rate in the pristine sample and a low index rate in the biaxial-deformed sample and the micrograph sizes are adjusted to display areas with relatively high index rates. Only one grain in the biaxial-deformed sample is well-resolved, so a grain with similar orientation and size is selected from the pristine results for direct comparison. The grain size in the pristine sample is 7.1 μm and the grain size in the biaxial-deformed sample is 5.7 μm, which are marked in Fig. 2 to show the grain orientations (a)–(b) and morphologies (c)–(d). The basal DAO of these grains are shown in Fig. 2 (d)–(f) with the basal orientations within ± 0.05° for the pristine grain and ± 1.5° for the biaxial-deformed grain.

The lattice strain components of the chosen pristine and biaxial-deformed grains are shown in Fig. 3 (a)–(f) using red and blue to indicate tension and compression, respectively. Histograms with Gaussian fits are included in Fig. 3 (g)–(i) to better quantify the strain variation which are significantly higher in the biaxial-deformed sample and display localized tension–compression variations compared to the pristine sample. The relationship between the trace lattice strains (HH, XX, FF) and the sample axes (RD, TD, ND), respectively, is provided in Fig. 1 (a). The lattice strain components are used to calculate the equivalent strains according to Eq. (2) and the a/c ratio variation assuming constant unit cell volume. The results of the equivalent strain and a/c ratio variation are shown in Fig. 4 for all indexed pixels (a)-(b) and the single grain analysis (c)-(d). Particularly within the single grain, the pristine sample displays narrow distributions of these metrics. The lattice parameters measured using the monobeam energy scans are $a = 0.32289$ (5) nm and $c = 0.51435$(5) nm which are similar to the results of pure zirconium [32]. The average (μ) and standard deviation (σ) fitting parameters for the distributions are listed in Table 2.

3.2. EBSD

Fig. 5 shows the microstructure characteristics of the pristine, biaxial-deformed, and uniaxial-deformed samples using micrographs with ND inverse pole figure (ND||IPF) coloring. Samples display typical CWSR texture with a strong basal-ND fiber indicated by the coloring in Fig. 5, and pole figures are included in the Supplementary materials to help quantify the texture (Fig. S4). The residual cold-worked microstructure from pilgering and annealing during manufacturing display similar characteristics to the deformation microstructure, so are collectively referred to as un-recrystallized (uRX) microstructure herein.

Multiple magnifications provide high resolution micrographs supported by micrographs with lower resolution but higher area to ensure statistical representation. At 600x magnification, thousands of grains are resolved in each micrograph compared to hundreds for the 4000x magnification. Grain numbers are included in Table 3 and micrograph areas are available in the Supplemental materials (Table S1). High resolution micrographs appear representative of the high area micrographs, but statistical data (texture, grain size, KAM, etc.) use the medium and high area data. Grains are elongated by approximately 50 % in the RD, and the uRX fraction is higher in the deformed sample compared to the pristine sample as listed in Table 3.

The band slope provides a metric of index quality which is high in RX grains and lower in the uRX microstructure (Figs. S6, S11 and S15). As the index quality decreases, it becomes insufficient for indexing and so the relatively low index rates of the uniaxial-deformed sample may affect the uRX fraction more than the RX fraction. To mitigate this, the analysis splits the microstructure into RX and uRX fractions for independent comparison (Fig. 9, Fig. 10, Table 3). Additional histograms and micrographs are available in the Supplementary materials to help visualize and quantify these characteristics (Figs. S5–S19).

Single grains from each sample marked in Fig. 5 are selected with similar orientations and sizes to those used in the 3DXM analysis to

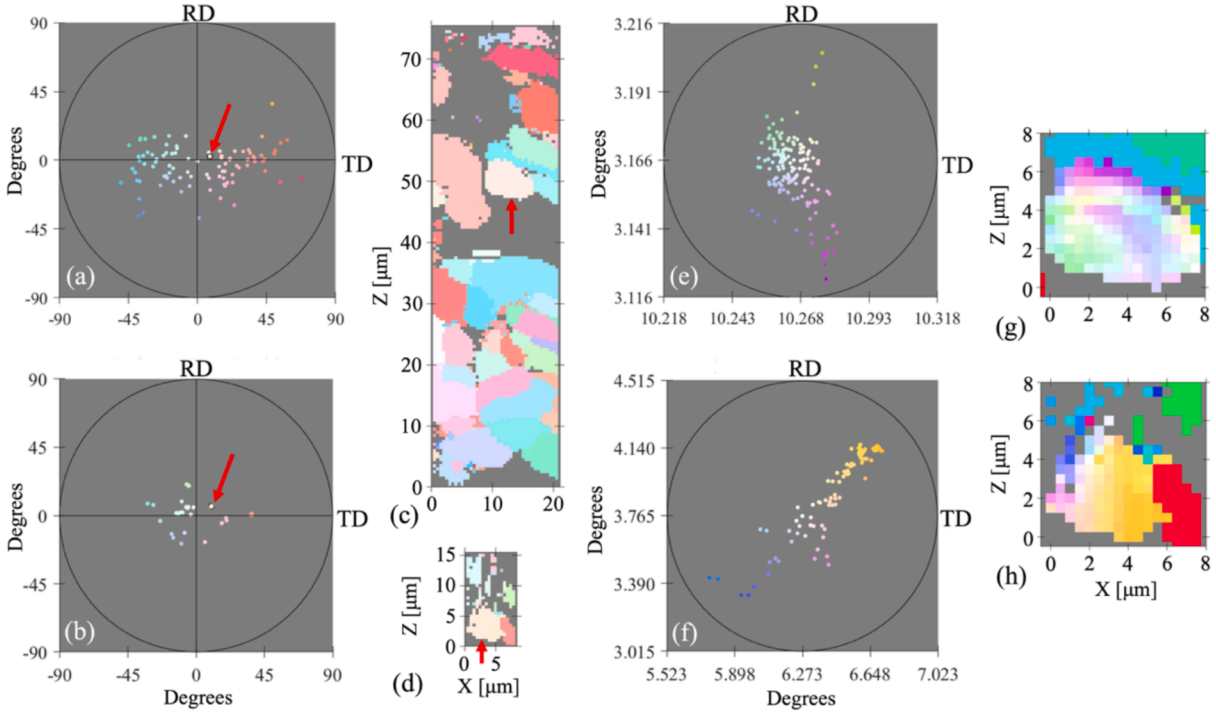

Fig. 2. Basal (00.2) orientation characteristics of the pristine (a), (c), (e), (g) and biaxial-deformed (b), (d), (f), (h) samples. ND pole figures show the texture (a)–(b) and intragranular disorientation (e)–(f) and provide the coloring used by the corresponding IPF micrographs of the illuminated plane, (c)–(d) and (g)–(h), respectively. Grains are marked using arrows in (a)–(d) for single grain analysis and (e)–(h) show the intragranular disorientation of each grain.

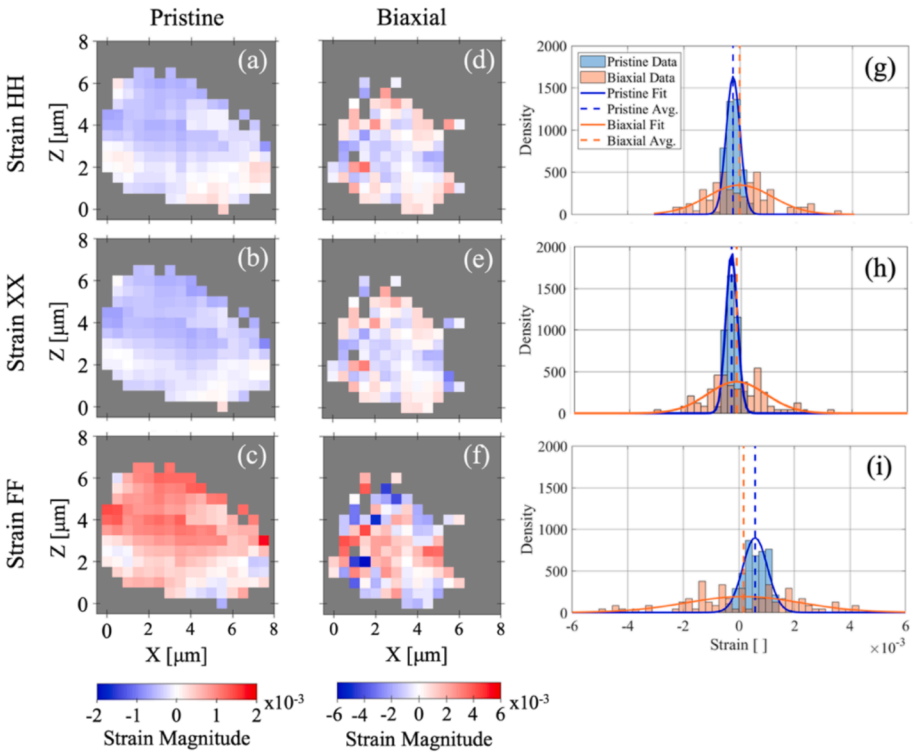

Fig. 3. Trace strain components of intragranular analysis shown using 2D micrographs (a)–(f) and probability density function histograms (g)–(i). Note the different limits of the color bars for the pristine (a)–(c) and biaxial-deformed (d)–(f) samples; the strain magnitude variation is more clearly shown point by point using the histograms (g)–(i). Red indicates tension and is shown as positive strain and blue indicates compression and is shown as a negative strain.

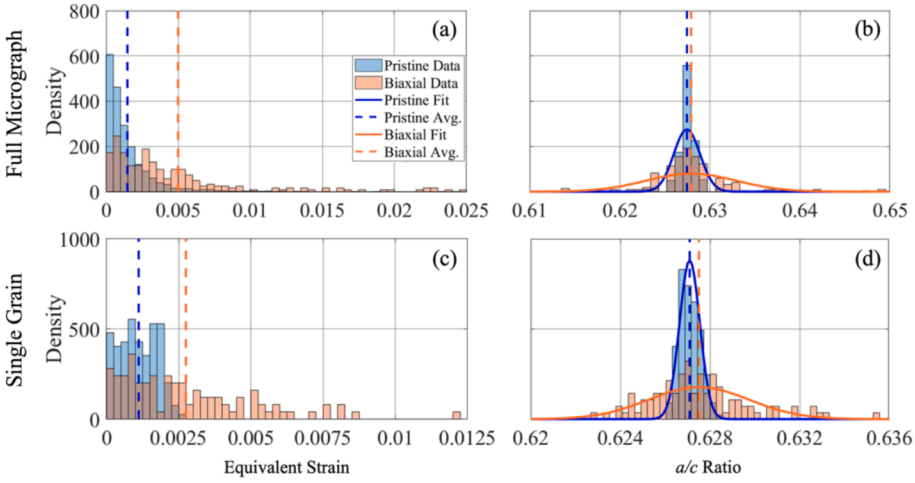

Fig. 4. Probability density histograms of the (a) von Mises lattice strain and (b) lattice parameter ratio of all indexed voxels. Corresponding values of single grains selected for analysis are plotted in (c) and (d).

compare results of both characterization methods. The pristine grain size is 6.31 μm, the biaxial-deformed grain size is 4.91 μm, and the uniaxial-deformed grain size is 5.08 μm; each grain has similar orientations to those used for the 3DXM single grains which are defined in the Supplementary materials (Fig. S20). The deformed grains display similar DAO and KAM compared to the pristine grain in Fig. 6, although both grains selected are RX with relatively low misorientation compared to uRX microstructure.

Grain size cumulative area fractions are shown in Fig. 7 at 4000x and 600x magnifications. The 600x magnification effectively captures large grains, while the 4000x magnification provides detailed resolution of small grains, ensuring a comprehensive analysis of the grain size distribution. The deformed samples display cumulative area fractions higher than the pristine area fraction up to about 9 μm, indicating a smaller grain size distribution. The uniaxial-deformed sample displays a grain size distribution similar to the biaxial-deformed sample with a slightly lower area fraction for intermediate sized grains.

High magnification KAM micrographs show orientation gradients present in pristine (a) and deformed (b)-(c) microstructures in Fig. 8. Typical areas are segmented to reveal representative deformation structures in detail, but the full micrographs are included in the Supplementary materials (Fig. S18). Fig. 8 (a) shows an area from the pristine sample, displaying typical undeformed RX grains with some residual uRX microstructure from manufacturing. The low-angle

Table 2
Mean (μ) and standard deviation (σ) of the strain and a/c ratio distributions shown in Fig. 3 and Fig. 4.

	Pristine		Biaxial-Deformed	
Single Grain	**μ**	**σ**	**μ**	**σ**
HH (RD) Strain × 10^{-3}	−0.25	0.24	−0.020	1.2
XX (TD) Strain × 10^{-3}	−0.33	0.21	−0.15	1.1
FF (ND) Strain × 10^{-3}	0.58	0.44	0.17	2.1
Equivalent Strain × 10^{-3}	1.11	–	2.75	–
a/c Ratio	0.6271	0.0005	0.6275	0.0023
Full Microstructure				
Equivalent Strain × 10^{-3}	1.47	–	4.99	–
a/c Ratio	0.6274	0.0015	0.6279	0.0050

orientation gradients in Fig. 8 (b) form walls around domains with low misorientation and in (c) many of these domains have achieved the necessary misorientation to classify as nanoscale sub-grains.

Similar to the previous single grain analysis, deformation in the microstructure is quantified using DAO and KAM but is assessed at different length scales on several microstructure categories: total, RX, and uRX. Grains larger than 1 μm with low intragranular misorientation are classified as RX grains, nanograins with low misorientation are classified as sub-grains, and the remaining microstructure with high misorientation are classified as uRX. The area fractions are reported in Table 3 and the intragranular deformation characteristics of these microstructure categories are compared using DAO and KAM histograms, as summarized in Fig. 9. The RX fraction decreases while the sub-grain and uRX fractions increase between the pristine and deformed samples, and similarly, the RX and DAO values are higher in the deformed samples compared to the pristine sample. However, the biaxial-deformed sample shows more significant changes in the total and RX categories compared to the pristine sample than the uniaxial-deformed sample does. No difference is observed in the uRX fraction between any of the samples. Additional micrographs are included in the Supplementary materials (Figs. S6–S19).

The RD texture shown in Fig. 10 display typical {10.0} fibers for the RX and uRX microstructure categories [4]. The uRX fiber is particularly strong and decreases from the pristine to the biaxial-deformed sample microstructures but increases from the pristine to the uniaxial-deformed sample microstructures. Multiple RX-uRX partitioning techniques are performed to ensure this effect is not an artifact of the higher misorientation in RX fraction of the biaxial-deformed sample, but these texture characteristics are consistent. Partitioning methods include the KAM-based methods described in Section 2 with results presented in Fig. 10, band slope filtering, and manual selection at 600x and 4000x magnification. Additional figures are provided in the Supplementary materials to help quantify these data (Fig. S21).

3.3. Simulation

The plastic spin is defined as the difference between the material spin and the lattice spin corresponding to rotation from plastic slip only [21,28]. Fig. 11 shows the VPSC simulation results of the plastic spin for the pristine microstructure at 600x magnification for different initial velocity tensors which Fig. 12 summarizes using histograms for all magnifications. The results using the macroscopic velocity gradient tensor defined by the biaxial strain rates display higher plastic spin

Table 3
Summary of EBSD data.

	Pristine		Biaxial-Deformed		Uniaxial-Deformed	
	600x	4000x	600x	4000x	600x	4000x
Index Rate:	77 %	90 %	81 %	82 %	49 %	75 %
Grain Count:	9288	674	10,672	1068	6489	932
Grain elongation – median:	1.51	–	1.43	–	1.64	–
Average:	1.45		1.50		1.09	
RX:	0.58	0.65	0.32	0.40	–	0.52
Area Fraction – sub-grain:	–	0.021	–	0.032	–	0.027
uRX:	–	0.32	–	0.55	–	0.43

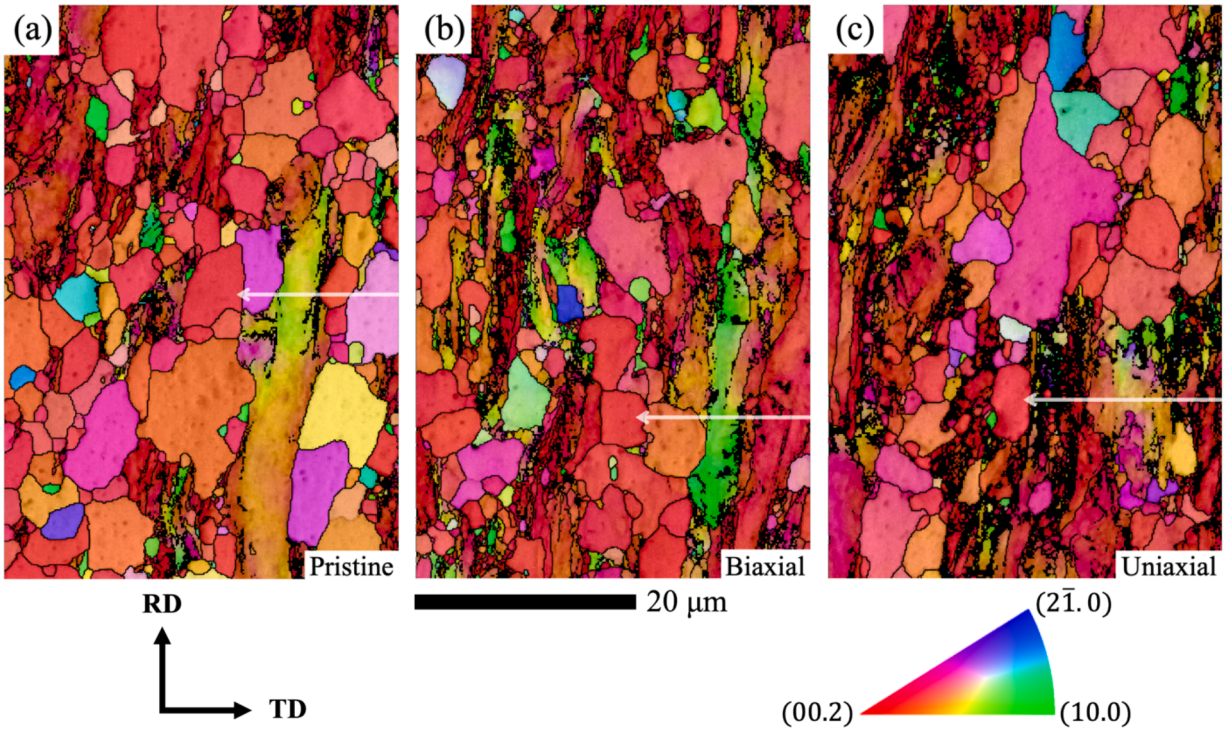

Fig. 5. EBSD ND||IPF micrographs for (a) pristine, (b) biaxial-deformed, and (c) uniaxial-deformed samples. Grain boundaries with more than 10° misorientation are marked with black lines and arrows in show grains selected for single grain analysis.

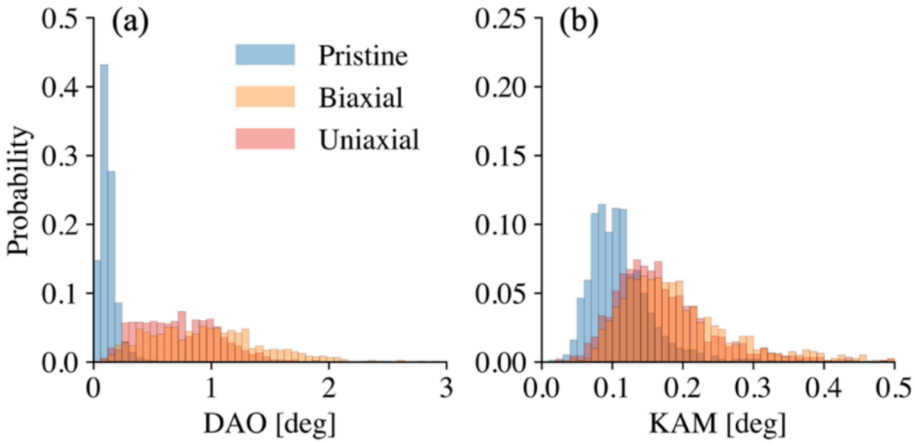

Fig. 6. Histograms of EBSD results for selected single grains marked in Fig. 5 showing (a) the DAO and (b) the KAM at 4000x magnification.

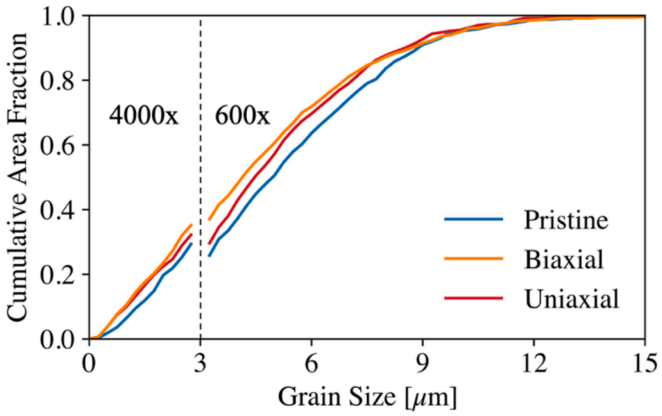

Fig. 7. Grain size distribution shown using the cumulative area fraction of each sample. Grain sizes below 3 μm are derived from the 4000x micrographs, while those above are from the 600x micrographs.

distributions compared to results defined by the uniaxial strain ratios while all other variables are constant. The applied velocity gradient tensors of both uniaxial tests are similar, particularly by including the same ND strain rate which is small compared to the biaxial velocity tensor. However, switching the tensile axis results in the uniaxial-TD simulation displaying higher plastic spin than the uniaxial-RD simulation, especially at higher magnifications with large area and reduced variability.

4. Discussion

In the present work, CWSR Zry-4 cladding is characterized in pristine and deformed states to evaluate microstructure changes from plastic deformation at elevated temperature. 3DXM and EBSD are used to quantify and visualize strains and misorientation in the material and comparable single grains are selected for more detailed analysis. Additionally, samples deformed using two loading modes are characterized with EBSD to clarify the effects of mechanical anisotropy on microstructure evolution. VPSC simulations are used to investigate differences in observed microstructures from identical initial conditions, considering only differences in the plastic strain rates from the relevant loading

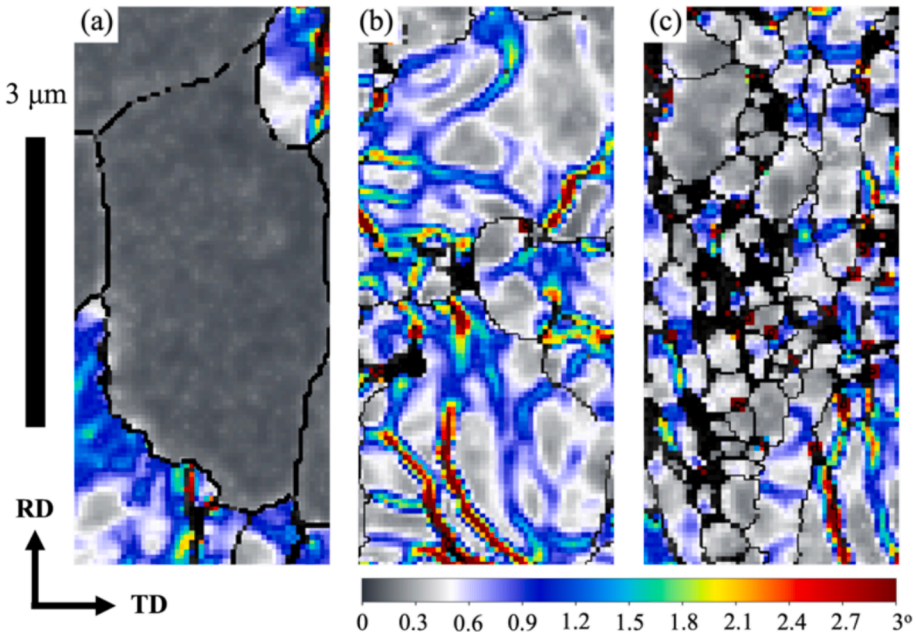

Fig. 8. High magnification (7500x) micrographs showing the KAM data for typical microstructure from the (a) pristine and (b)–(c) biaxial-deformed samples.

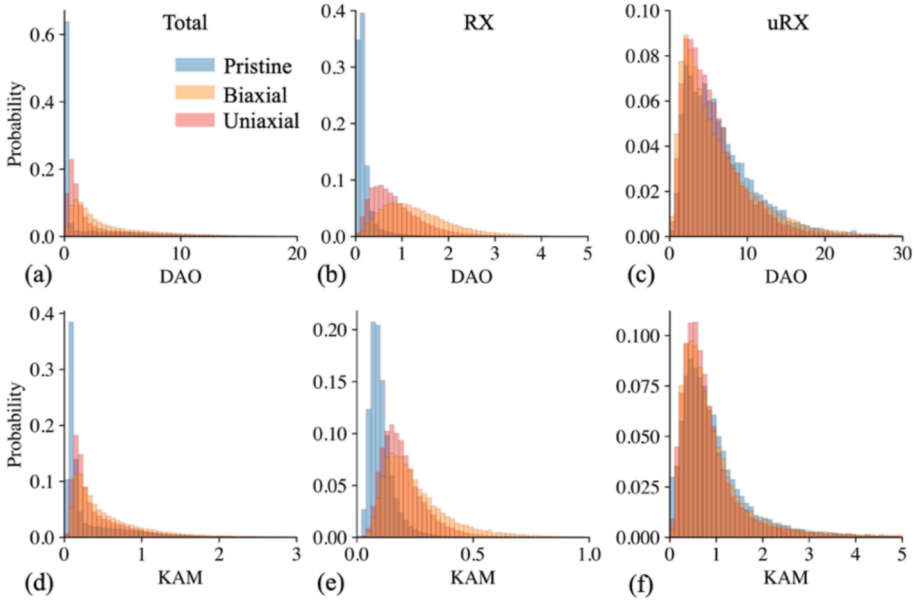

Fig. 9. Total, RX, and uRX misorientation characteristics quantified using (a)–(c) DAO at 600x magnification and (d)–(f) KAM at 4000x magnification.

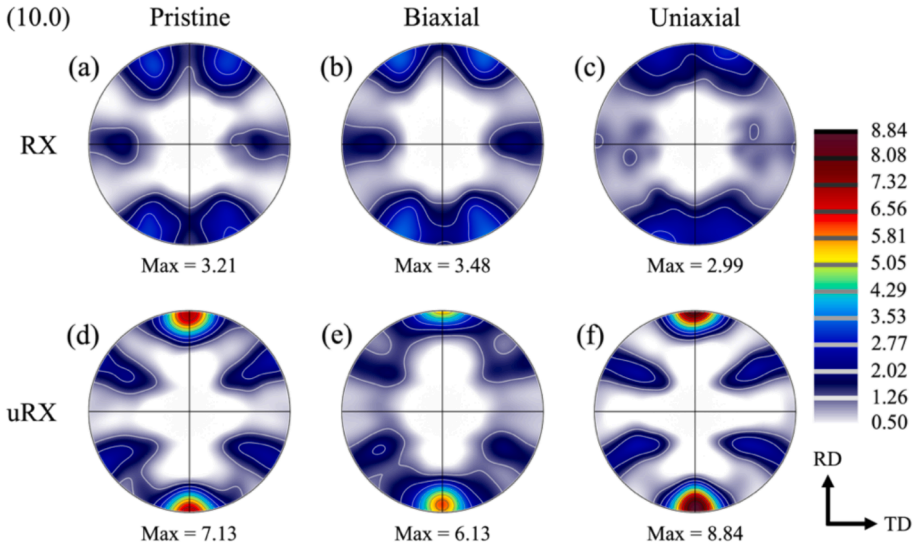

Fig. 10. Prismatic (10.0) texture of the (a)–(c) RX and (d)–(f) uRX fractions for each sample at 600x.

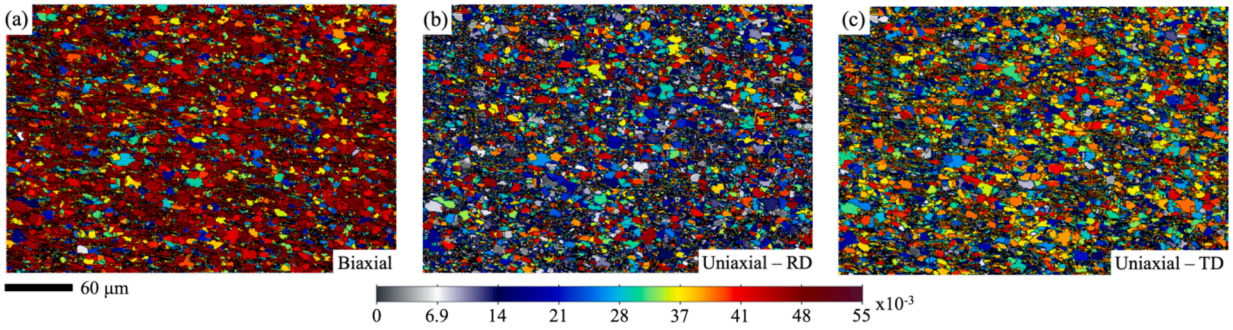

Fig. 11. Micrographs showing the VPSC simulation plastic spin results at 600x magnification for the (a) biaxial, (b) uniaxial-RD, and (c) uniaxial-TD velocity tensors.

mode.

Variables such as sample preparation, interaction volume, and residual strains are some of the important key-role factors affecting the index rate of both characterization methods. Both characterization techniques most successfully resolve RX microstructure where large grains and low misorientation provide the strongest diffraction

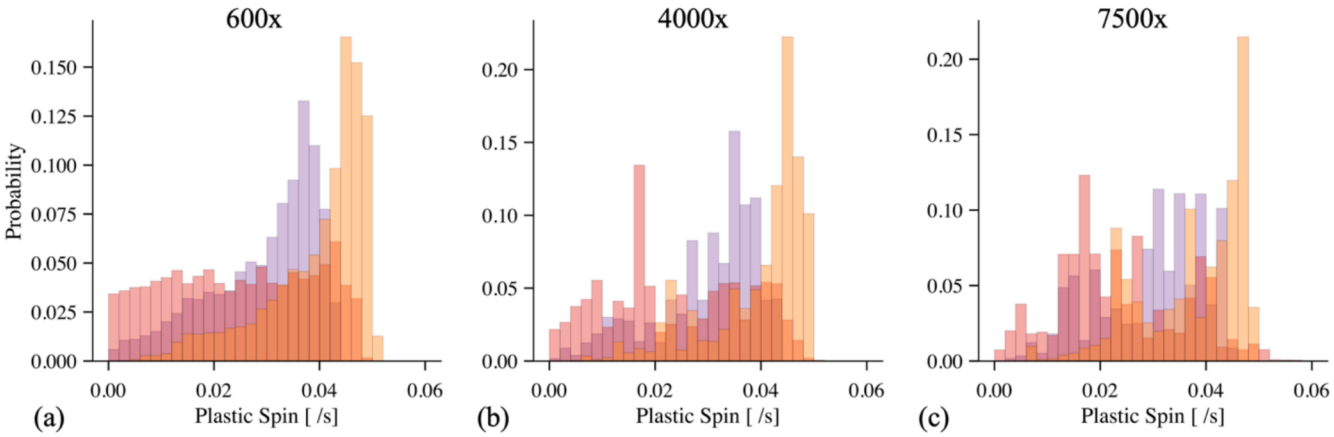

Fig. 12. Histograms summarizing the VPSC simulation plastic spin results at (a) 600x (b) 4000x, and (c) 7500x magnification. Note that higher magnification and reduced area introduces variability in the distributions.

conditions. The deformed samples retain some of the RX grains, but their area fraction is smaller, and the DAO, lattice strains, and KAM values are higher compared to the pristine sample. The single grain analysis highlights this, revealing significant differences between grains which first appear similar. The DAO measured in single RX grains using 3DXM and EBSD techniques are comparable, demonstrating that these methods are consistent and provide complementary datasets.

The EBSD results indicate that macroscopic plastic deformation is accommodated by microscopic strain gradients leading to grain fragmentation. The pristine sample grain size area fraction in Fig. 7 slightly shifts towards smaller grains for the deformed samples, suggesting that larger grains fragment into multiple smaller sub-grains upon plastic deformation. The area fraction results of the microstructure categories listed in Table 3 support this finding, with a modest increase in sub-grain area indicating a much larger increase in the number of sub-grains. Fig. 8 uses KAM to highlight misorientation indicative of strain which, at high magnification, display structures defining low misorientation domains.

Orientation gradients and grain fragmentation revealed in the deformation microstructure indicate that plastic spin may be an active deformation mode. Fig. 13 shows the relationship between these schematically with pristine microstructure which is deformed by an imposed strain (∈). The material spin (β) and lattice spin (Ω) are similar in area A, which minimizes the difference between them: the plastic spin. Grains often rotate by a common lattice spin but may be constrained and develop intragranular cells where the lattice spin varies and the plastic spin is high, such as shown in Fig. 13 (b) area B [17]. Boundaries where intragranular lattice spin is different are shown with dashed lines which are measured as KAM with EBSD characterization.

The effect of plastic spin, shown in Fig. 13 (b) area B, is captured experimentally and visualized in Fig. 14. Fig. 14 (a) uses KAM to display orientation gradients forming boundaries of varying intragranular lattice spin, (b) displays the disorientation axis from the average grain orientation to show the relative lattice spin direction, and (c) overlays both to show their relationship. These structures are similar in size and shape to the dislocation cell structures observed with transmission electron microscopy in similarly deformed Zircaloys, which displayed dense dislocation walls surrounding low dislocation density domains [11,33,34].

The relationship between lattice spin and deformation-induced texture development shown in Fig. 10 is clarified by experimental and VPSC simulation results of texture development from Xu et al. [35] for a similarly textured Zircaloy, so no texture evolution simulations are performed in the present study. Xu et al. [35] show that tensile strains in the RD and TD produce {10.0} fibers in the axis of high tensile stress and plastic strain. The plastic strain ratios in Table 1 show that axial tension loading produces a high plastic strain rate in the RD, whereas internal pressure loading produces a high plastic strain rate in the TD. Consequently, axial tension loading develops uRX microstructure with a {10.0} fiber in the RD, increasing the similar uRX texture from pilgering. Conversely, internal pressure loading develops uRX microstructure with $\{2\bar{1}.0\}$ fiber in the RD, which differs from the pilgering uRX texture and decreases the texture intensity. The differences in textures are small, but the trends agree with the results of [35]. An analysis of Schmid factors reveals no difference between {10.0} and $\{2\bar{1}.0\}$ RD fibers associated with the pilgered uRX and RX microstructures that might affect the

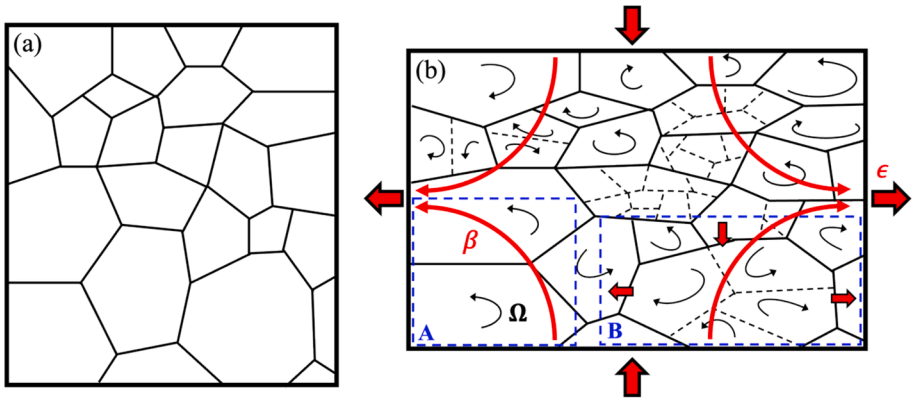

Fig. 13. Schematic representation of (a) pristine microstructure which is (b) deformed by tension in the horizontal direction. Grain boundaries are shown as solid black lines, orientation gradients are shown with dashed black lines, material spin is shown as red arrows, and lattice spin is shown as black arrows.

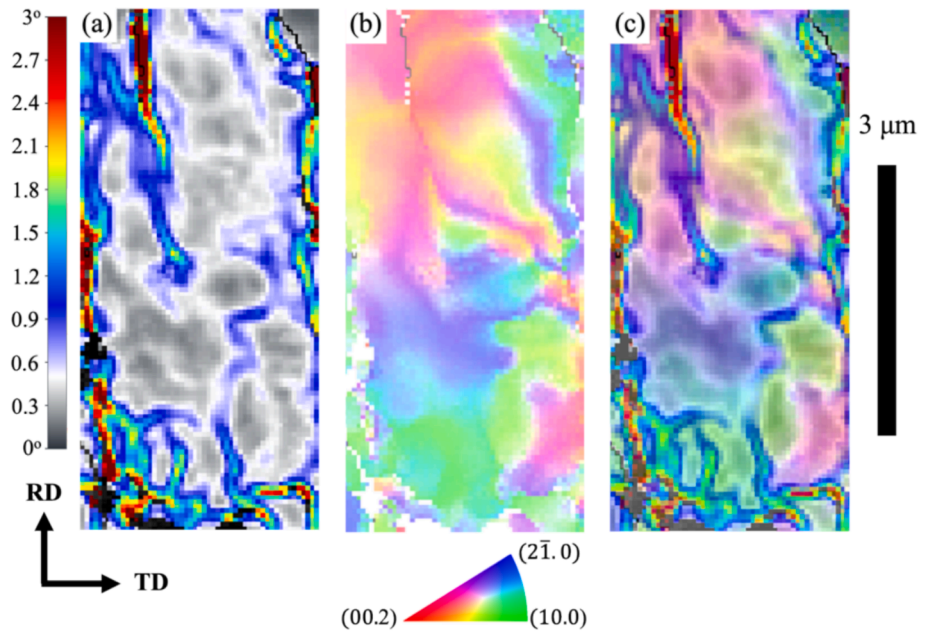

Fig. 14. Micrographs of a grain from the biaxial-deformed sample at high magnification (7500x). (a) A KAM micrograph highlighting orientation gradients, (b) the disorientation axis from the average grain orientation defined using ND||IPF coloring, and (c) the disorientation axis micrograph superimposed with 66% transparency on the KAM micrograph to show their relationship.

differences in misorientation observed between the biaxial-deformed or uniaxial-deformed samples.

Yang et al. [34] used transmission electron microscopy to correlate dislocation cells to dynamic recovery in highly deformed zircaloy because dislocation annihilation exceeds nucleation. Similar dislocation cells in the present uRX microstructure suggest that the dislocation density reaches the threshold required for dynamic recovery [34]. Considering this, dynamic recovery can account for the similarities between pristine and deformed uRX microstructure data in Fig. 9 (c) and (f), suggesting a similar threshold for static recovery during the CWSR annealing. In contrast, dislocation nucleation exceeds annihilation in the RX microstructure, as shown by clear differences between the pristine and deformed samples in Fig. 9 (b) and (e). Evidence of dynamic recovery with a similar threshold to static recovery suggests that, in samples deformed *via* internal pressurization, the increased uRX fraction does not significantly contribute to enhanced relaxation while the higher misorientation in the RX fraction could affect results in [16]. These differences in the RX microstructure and the microstructure area fractions reveal that the biaxial-deformed sample displays more deformed characteristics than the uniaxial-deformed sample, consistent with the observations made in [16]. To provide stronger confirmation that this effect results from the plastic strain ratios instead of increased hardening, samples with different strains are used in the present work. The results indicate that internal pressure loading accelerates the misorientation accumulated in RX microstructure, and differences in the RD, TD, and ND strain rates between loading modes are analyzed to better understand this phenomenon.

The VPSC simulations show that the plastic spin results of the internal pressure and axial tension velocity tensors are consistent with the increased misorientation observed in the biaxial-deformed sample microstructure. Bunge & Nielsen [17] performed extensive mechanical testing and texture analysis, revealing that the plastic spin is minimized when the symmetry of imposed deformation is parallel to the symmetry of the initial texture and is highest when deformation is imposed at the "most asymmetric" tensile directions. In this study, axial loading is colinear with the symmetric RD axis and simulations predict the least plastic spin. The uniaxial-TD simulations predict slightly higher plastic spin indicating that results are sensitive the loading orientation with respect to the texture symmetry independently of uniaxial versus biaxial loading. Internal pressure loading imposes biaxial loads in the RD and TD and the simulation predicts the highest plastic spin, indicating that biaxial loading is the least symmetric. The texture evolution discussed in the previous paragraph reflects the differences in plastic spin, and the resulting misorientation. Specifically, the material spin more closely matches the lattice spin for the axial tension mode compared to the internal pressure mode, thereby reducing the plastic spin.

5. Conclusions

Conclusions from the microstructure characterization and analysis of CWSR Zry-4 cladding performed in this study at 400 °C are summarized below:

1. Deformation increases intragranular misorientation in RX microstructure while dislocation production exceeds annihilation.
2. High misorientation associated with uRX microstructure is limited by dynamic recovery which form structures that appear to be dislocation cells formed by plastic spin. Further deformation increases cell misorientation until they are classified as sub-grains.
3. Residual uRX microstructure from pilgering and deformation induced uRX microstructure are similar, indicating that static recovery during annealing has a similar limit to dynamic recovery during deformation at 400 °C.
4. Strain from uniaxial tension in the RD produces a {10.0} texture fiber in the RD like uRX microstructure from pilgering, increasing the uRX fiber intensity. Strain from internal pressurize produces a {2$\bar{1}$.0} texture fiber in the RD, reducing the uRX fiber intensity.
5. Internal pressure loading produces high plastic spin compared to uniaxial loading along the RD. Consequently, the biaxial-deformed sample displays increased deformation microstructure at lower imposed strain compared to the uniaxial-deformed sample.

This investigation provides evidence at multiple length scales that biaxial loading relevant to PCI conditions produces increased deformation microstructure compared to samples tested with uniaxial loading along the RD. Microstructure characterization results are supported by

VPSC simulations indicating that the deformation microstructure is sensitive to the anisotropy observed in textured Zircaloy and that the uniaxial-deformed microstructure may not be representative of the PCI conditions for sensitive analysis. Analysis suggests that internal pressure loading is a relatively low symmetry loading mode compared to loading parallel to the RD which develops relatively high plastic spin that is observed as increased misorientation in the microstructure.

Disclosure statement

This information was prepared as an account of work sponsored by an agency of the U.S. Government. Neither the U.S. Government nor any agency thereof, nor any of their employees, makes any warranty, express or implied, or assumes any legal liability or responsibility for the accuracy, completeness, or usefulness of any information, apparatus, product, or process disclosed, or represents that its use would not infringe privately owned rights. References herein to any specific commercial product, process, or service by trade name, trademark, manufacturer, or otherwise, does not necessarily constitute or imply its endorsement, recommendation, or favoring by the U.S. Government or any agency thereof. The views and opinions of authors expressed herein do not necessarily state or reflect those of the U.S. Government or any agency thereof.

CRediT authorship contribution statement

Malachi Nelson: Writing – review & editing, Writing – original draft, Visualization, Methodology, Investigation, Formal analysis, Conceptualization. **Shmuel Samuha:** Writing – review & editing, Visualization, Methodology, Investigation, Formal analysis, Conceptualization. **Dina Sheyfer:** Writing – review & editing, Visualization, Methodology, Investigation, Formal analysis. **David Kamerman:** Writing – review & editing, Supervision, Resources, Methodology, Investigation, Funding acquisition, Conceptualization. **David Yang:** Writing – review & editing, Supervision, Resources, Methodology, Investigation, Funding acquisition, Conceptualization. **Kay Song:** Writing – review & editing, Visualization, Investigation. **Felix Hofmann:** Writing – review & editing, Supervision, Investigation, Funding acquisition. **Jon Tischler:** Supervision, Methodology, Investigation. **Peter Hosemann:** Writing – review & editing, Supervision, Resources, Conceptualization.

Declaration of competing interest

The authors declare that they have no known competing financial interests or personal relationships that could have appeared to influence the work reported in this paper.

Acknowledgements

This work was supported through the U.S. Department of Energy (DOE) Advanced Fuels Campaign under DOE Idaho Operations Office contract DE-AC07-05ID14517. Work at Brookhaven National Laboratory was supported by the U.S. Department of Energy, Office of Science, Office of Basic Energy Sciences, under Contract No. DESC0012704.

Use of the Advanced Photon Source was supported by the U. S. Department of Energy, Office of Science, Office of Basic Energy Sciences, under Contract No. DE-AC02-06CH11357. Data was collected on the X-ray Laue diffraction beamline 34-ID-E under GUP 76902 at the Advanced Photon Source, Argonne National Laboratory.

Data availability

Data will be made available on request.

References

[1] K.J. Geelhood, "Fuel Performance Considerations and Data Needs for Burnup above 62 GWd/MTU In-Reactor Performance, Storage, and Transportation of Spent Nuclear Fuel," Pacific Northwest National Laboratory, Richland, Washington 99352, PNNL-29368, 2019.
[2] J.D. Hales, et al., BISON Theory Manual The Equations behind Nuclear Fuel Analysis, United States (Sep. 2016), https://doi.org/10.2172/1374503.
[3] E. Tenckhoff, *DEFORMATION MECHANISMS, AND ANISOTROPY IN ZIRCONIUM AND ZIRCALOY*, ASTM Int, 1988.
[4] K.L. Murty, I. Charit, Texture development and anisotropic deformation of zircaloys, *Prog. Nucl. Energy* 48 (4) (2006) 325–359, https://doi.org/10.1016/j.pnucene.2005.09.011.
[5] C. Lemaignan, *Zirconium Alloys: Properties and Characteristics* vol. 2 (2012) 232.
[6] C.L. Whitmarsh, "Review of Zircaloy-2 and Zircaloy-4 Properties Relevant to N.S. Savannah Reactor Design," ORNL-3281, 1962. [Online]. Available: DOI: 10.2172/4827123.
[7] G. Bharat Reddy, A. Sarkar, R. Kapoor, A.K. Kanjarla, Effect of temperature on the selection of deformation modes in Zircaloy-4, Mater. Sci. Eng. A 734 (Sep. 2018) 210–223, https://doi.org/10.1016/j.msea.2018.07.094.
[8] S. Deng, H. Song, H. Liu, S.H. Zhang, Effect of uniaxial loading direction on mechanical responses and texture evolution in cold pilgered Zircaloy-4 tube: Experiments and modeling, *Int. J. Solids Struct.* 213 (2021) 63–76, https://doi.org/10.1016/j.ijsolstr.2020.12.015.
[9] W. Guo, et al., Texture development and mechanical behavior of Zircaloy-4 alloy plates fabricated by cold rolling and annealing, *Mater. Sci. Eng. A* 807 (September) (2020) 140846, https://doi.org/10.1016/j.msea.2021.140846.
[10] N. Kumar, A. Alomari, K.L. Murty, Understanding thermally activated plastic deformation behavior of Zircaloy-4, *J. Nucl. Mater.* 504 (Jun. 2018) 41–49, https://doi.org/10.1016/j.jnucmat.2018.03.031.
[11] H. Shi, et al., The progressive intensification and attenuation of yield point phenomenon in a new polycrystalline zirconium alloy : Anisotropic response of work hardening-softening transition, *Mater. Sci. Eng. A* 848 (June 2022) 143385, https://doi.org/10.1016/j.msea.2022.143385.
[12] F. Xu, R.A. Holt, M.R. Daymond, Modeling lattice strain evolution during uniaxial deformation of textured Zircaloy-2, *Acta Mater.* 56 (14) (Aug. 2008) 3672–3687, https://doi.org/10.1016/j.actamat.2008.04.019.
[13] M. Suzuki, T. Fuketa, H. Saitou, Analysis of pellet-clad mechanical interaction process of high-burnup PWR fuel rods by RANNS code in reactivity-initiated accident conditions, *Nucl. Technol.* 155 (3) (2006) 282–292, https://doi.org/10.13182/NT06-A3762.
[14] Y. Udagawa, T. Sugiyama, M. Suzuki, F. Nagase, Stress biaxiality in high-burnup PWR fuel cladding under reactivity-initiated accident conditions, *J. Nucl. Sci. Technol.* 50 (6) (Jun. 2013) 645–653, https://doi.org/10.1080/00223131.2013.787030.
[15] M. Nelson, S. Samuha, D. Kamerman, P. Hosemann, Temperature-Dependent Mechanical Anisotropy in Textured Zircaloy Cladding, *J. Nucl. Mater.* 595 (Jul. 2024) 155045, https://doi.org/10.1016/j.jnucmat.2024.155045.
[16] M. Nelson, S. Samuha, B. Kombaiah, D. Kamerman, and P. Hosemann, "Enhanced Stress Relaxation Behavior via Basal <a> Activity from Internal Pressure Loading in Zircaloy-4 Cladding," *J. Nucl. Mater.*, vol. Unpublished Work, Submitted, 2024.
[17] H.J. Bunge, I. Nielsen, Experimental determination of plastic spin in polycrystalline materials, *Int. J. Plast.* 13 (5) (Jan. 1997) 435–446, https://doi.org/10.1016/S0749-6419(97)00018-1.
[18] Y.F. Dafalias, M.M. Rashid, The effect of plastic spin on anisotropic material behavior, *Int. J. Plast.* 5 (3) (Jan. 1989) 227–246, https://doi.org/10.1016/0749-6419(89)90014-4.
[19] C.R. Song, G.Z. Voyiadjis, Microstructure consideration with plastic spin and multiple back-stresses for large strain problems in soils, *Int. J. Plast.* 18 (10) (Oct. 2002) 1271–1289, https://doi.org/10.1016/S0749-6419(01)00069-9.
[20] H.M. Zbib, E.C. Aifantis, On the concept of relative and plastic spins and its implications to large deformation theories. Part II: Anisotropic hardening plasticity, *Acta Mech.* 75 (1) (Dec. 1988) 35–56, https://doi.org/10.1007/BF01174626.
[21] B. Beausir, L.S. Tóth, K.W. Neale, Role of strain-rate sensitivity in the crystal plasticity of hexagonal structures, *Int. J. Plast.* 23 (2) (Feb. 2007) 227–243, https://doi.org/10.1016/j.ijplas.2006.02.013.
[22] K.-C. Lan, et al., The challenge of acquiring a satisfactory EBSD result of CWSR Zircaloy-4 cladding tube, *J. Microsc.* 272 (1) (2018) 25–34, https://doi.org/10.1111/jmi.12729.
[23] D. Kamerman, M. Nelson, Multiaxial Plastic Deformation of Zircaloy-4 Nuclear Fuel Cladding Tubes, Nucl. Technol. (Feb. 2023) 1–15, https://doi.org/10.1080/00295450.2022.2160174.
[24] F. Dunne, N. Petrinic, *Introduction to Computational Plasticity*, Oxford University Press, 2005.
[25] J.D. Budai, et al., Polychromatic X-ray micro- and nanodiffraction for spatially-resolved structural studies, Proc. EMRS 2007 Fall Meet. Symp. H Curr. Trends Opt. X-Ray Metrol, Adv. Mater. Devices II Wars. Pol. 516 (22) (Sep. 2008) 8013–8021, https://doi.org/10.1016/j.tsf.2008.04.045.
[26] W. Liu G.E. Ice B.C. Larson W. Yang J.Z. Tischler J.D. Budai "The Three-Dimensional X-ray Crystal Microscope: A New Tool for Materials Characterization", 2004.
[27] R. Barabash, *Strain and Dislocation Gradients from Diffraction*, IMPERIAL COLLEGE PRESS (2014), https://doi.org/10.1142/p897.
[28] B. Beausir and J.J. Fundenberger, "Analysis Tools for Electron and X-ray diffraction," *ATEX-Softw.*, 2017, [Online]. Available: www.atex-software.eu.

[29] Y. Wang, K.L. Murty, Effect of Temperature on Mechanical Anisotropy of Zircaloy-4 Sheet, *Met. Mater.* 4 (4) (1998) 723–726, https://doi.org/10.1007/BF03026387.
[30] S. Wang, F. Giuliani, T.B. Britton, Variable temperature micropillar compression to reveal basal slip properties of Zircaloy-4, *Scr. Mater.* 162 (Mar. 2019) 451–455, https://doi.org/10.1016/j.scriptamat.2018.12.014.
[31] J. Gong T.B. Britton M.A. Cuddihy F.P.E. Dunne A.J. Wilkinson "Prismatic, basal, and slip strengths of commercially pure Zr by micro-cantilever tests" 96 2015 249 257 10.1016/j.actamat.2015.06.020.
[32] A.I. Kolesnikov, A.M. Balagurov, I.O. Bashkin, A.V. Belushkin, E.G. Ponyatovsky, M. Prager, Neutron scattering studies of ordered gamma -ZrD, *J. Phys. Condens. Matter* 6 (43) (1994) 8977, https://doi.org/10.1088/0953-8984/6/43/004.
[33] R.J. McCabe, E.K. Cerreta, A. Misra, G.C. Kaschner, C.N. Tomé, Effects of texture, temperature and strain on the deformation modes of zirconium, *Philos. Mag.* 86 (23) (2007) 3595–3611, https://doi.org/10.1080/14786430600684500.
[34] Z.N. Yang, F.C. Zhang, Y.Y. Xiao, Z.G. Yan, Dynamic recovery: The explanation for strain-softening behaviour in Zr–2.3Nb alloy, *Scr. Mater.* 67 (12) (Dec. 2012) 959–962, https://doi.org/10.1016/j.scriptamat.2012.08.026.
[35] F. Xu, R.A. Holt, M.R. Daymond, Modeling texture evolution during uni-axial deformation of Zircaloy-2, *J. Nucl. Mater.* 394 (1) (Oct. 2009) 9–19, https://doi.org/10.1016/j.jnucmat.2009.07.006.